RSC Advances

PAPER

View Article Online
View Journal | View Issue

Cite this: *RSC Adv.*, 2024, **14**, 7564

Photoacoustic detection of transient phase transformation of nanoparticles†

Shiqi Lv, Jiawei Li, Haotian Wang and Huiwu Yu *

The controllable preparation of spherical micro/nano particles of various materials has been achieved *via* the technology of the laser synthesis and processing of colloids (LSPC) recently. However, there is limited *in situ* research on the evolution processes of nanoparticles in photothermal transient environments, such as solid-state crystal transformations and changes of state, which limits the understanding and application of LSPC. Photoacoustic (PA) signals are sensitive to the optical, thermal and elastic properties of the medium, and can be used to measure the thermal and spectroscopic properties of matter. In this paper, the PA signals generated by the interaction of the laser with the surrounding liquid medium (ethanol, water, glycerin, *etc.*) and nanoparticles (Ag, TiO_2, CeO_2, ZrO_2, *etc.*) are studied when the tunable LSPC technique provides different photothermal conditions (such as thermal expansion, solid crystal transformation and evaporation). It is found that semiconductors with different bandgaps, as light absorbers, have the ability to selectively absorb laser beams of different wavelengths. By changing the wavelength, the PA intensity can be adjusted accordingly. In addition, based on the fast laser heating and tunable fluence characteristics of non-focused laser beams in LSPC technology, transient processes such as material phase transitions and changes of state can be excited separately by adjusting the laser fluence. Taking titanium dioxide as an example, the PA signals generated by laser selective excitation of A–R (anatase into rutile) phase transitions and rutile vaporization can be detected.

Received 15th January 2024
Accepted 22nd February 2024

DOI: 10.1039/d4ra00383g

rsc.li/rsc-advances

Introduction

In recent years, significant progress has been made in the technology of laser synthesis and processing of colloids (LSPC) for the controllable preparation of micro/nano materials,[1–5] such as the composition of products ranging from unit metals to metal oxides and multiple alloys,[6–9] the size of products ranging from submicron to nanoscale,[10–12] the state of matter of products ranging from solid to liquid alloys,[13–15] the structure of products ranging from solid to hollow and core–shell particles,[16–20] and the morphology of products ranging from spherical to non-spherical.[21–23] The melting-evaporation mechanism proposed by Pyatenko A. *et al.* successfully explained the relationship between laser fluence and product size during the process of irregular particles entering the sphere in materials.[24,25] In addition, based on the extended photothermal evaporation mechanism, problems such as alloy product segregation have also been successfully explained.[15] However, there is limited *in situ* research on the evolution processes of nanoparticles in photothermal transient environments, such as solid-state crystal transformations and changes of state, which limits the understanding and application of LSPC technology. Recently, various methods of real-time analysis, such as *in situ* X-rays,[26,27] dynamic light scattering (DLS),[28] light absorption/emission spectroscopy,[29,30] time-resolved shadowgraphy,[31,32] photoacoustic (PA) spectroscopy[33–36] are used to analyze the process of laser interaction with matter. DLS provides information on the presence of a few nm or larger objects,[37] however, this technology does not distinguish between bubbles and nanoparticles, and the signal is strongly dominated by larger objects.[38] Light absorption/emission spectroscopy and time-resolved shadowgraphy provides evolution information of micro/nano materials and liquids during laser irradiation,[39,40] but there are limitations in measuring opaque samples. PA spectroscopy can be performed with a time resolution of the order of 10^{-6} s and provides information on the time evolution of shockwaves.[41] PA spectroscopy is a technology that studies the thermal properties (thermal conductivity, thermal diffusivity, specific heat, *etc.*) and spectroscopic properties of materials through the detection of acoustic signals generated by laser interaction with materials.[42–45] Due to the low interference of reflected light and scattered light, and the good penetration of acoustic signal, PA spectroscopy can be used for the determination of opaque samples, such as gel, sol, powder, biology, *etc.*[46–50]

School of Physics, Northwestern University, Xi'an 710127, China

† Electronic supplementary information (ESI) available. See DOI: https://doi.org/10.1039/d4ra00383g

The PA study of colloidal solutions or biomass systems using solid nanoparticles as photothermal conversion agents has broad application prospects in fields such as imaging and photothermal therapy. When nanoparticles are used as PA contrast agents, the absorbed energy by the nanoparticles can lead to thermal expansion locally within the particle, and in the surrounding fluid, to which the absorbed energy is transferred. However, at present, most studies focus on the PA signals generated by the expansion and vaporization of liquid phase media, and there is relatively little research on the phase transition and vaporization of nanoparticles. At present, many studies have focused on PA signals produced by liquid media.[36,51,52] During the interaction between laser and nanoparticles, the electrons in matter absorb light at approximately the femtosecond scale, and then the electrons transfer the absorbed energy to the lattice.[53] Thermal elastic expansion and phase transition of the nanoparticles in ps–ns.[54] The melting[55] and evaporation[56] processes where nanoparticles absorb more heat energy are approximately on the ns–μs time scale. With further extension of time, a large amount of energy diffuses from the nanoparticles to the surrounding liquid phase medium, leading to vaporization of the liquid phase medium at the μs scale.[57] As a result, due to limitations such as the propagation speed of sound waves in the liquid phase medium and the bandwidth (<100 MHz) of piezoelectric transducers (PZTs), it is still a huge challenge to directly detect and distinguish the changes in the nanoparticles and liquid phase medium during the aforementioned photothermal processes in the time domain.

Herein, LSPC technology was used to irradiate micro/nano materials with different properties such as silver, titanium oxide, and alumina. Based on the photothermal mechanism and the adjustability of laser fluence, controllable preparation of micro/nano materials had been achieved. Simultaneously, PA signals were collected that may include information on transient photothermal processes such as nanoparticles thermal expansion, crystal phase transition, and changes of state. Subsequently, scanning electron microscopy (SEM), transmission electron microscopy (TEM), and Raman spectroscopy were used to analyze the changes in the morphology and crystal structure of the nanoparticles before and after laser irradiation. A systematic exploration was conducted on the relationship between the intensity of PA signals during laser irradiation and the crystal transformation, evaporation, and other processes of the nanoparticles.

Experimental

The schematic diagram of the experimental device for preparing nanoparticles using LSPC and collecting PA signals is shown in Fig. 1a. In the experiment, an appropriate amount of nano material was first dispersed in the solvent through ultrasound to obtain a precursor solution with a concentration of 0.02 mg ml^{-1}. Next, the dispersed solution was transferred to a PA reaction cell (6 cm × 6 cm × 6 cm, square glass dish), irradiated with unfocused pulse laser (Nd:YAG, repetition frequency 10 Hz, pulse width 7 ns, beam diameter 5 mm). The laser beam

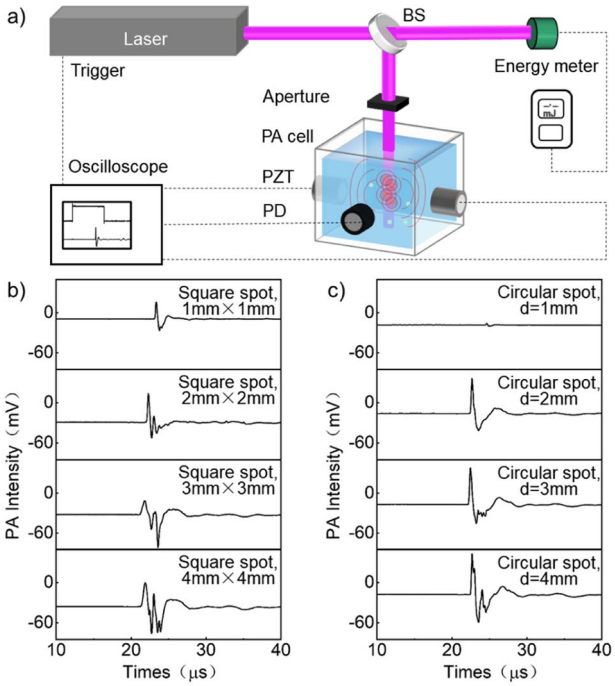

Fig. 1 (a) The schematic diagram of the experimental device for preparing nanoparticles using LSPC and collecting PA signals. PA signals generated by the square spot (b) and circular spot (c) with different sizes.

was split a beam splitter (BS), with the reflected beam (90%) entering the PA cell for reaction, and the transmitted beam (10%) entering the energy meter for energy monitoring. PZTs (20 MHz, bandwidth about 80%, model I20-6SJ) were used to collect PA signals by directly contacting the reaction medium through holes penetrating the sidewall of the PA cell. In addition, a photodetector (PD) was placed by the PA cell to monitor the scattered beam signal of the laser. The collection and processing of PA signals and PD signals were carried out employing a digital oscilloscope (SDS2354XPlus, Dingyang). The influence of the size and shape of the laser beam spot on the PA signal is shown in Fig. 1b and c. As shown in the figure, the smaller the size of the laser beam spot, the narrower the peak width of the PA signal (shorter the time) generated by square and circular spots. When the size of the spot is greater than 1 mm, the peak-to-peak intensity of the PA signal generated by the square spot and the circular spot are approximate. The PA signal intensity of the circular spot with a diameter of 1 mm is weaker, while the PA signal intensity of the square spot with a size of 1 mm × 1 mm is stronger. Therefore, 1 mm × 1 mm square spot was used in this experiment.

Results

The PA signals of silver nanoparticles in different solvents (glycerol, deionized water, kerosene, ethanol, acetone) are shown in Fig. 2a. The rising edge of the laser output signal was served as the trigger signal (Fig. 2a(I)), and a signal of about 1.5 μs was the signal of the pulse laser (Fig. 2a(II)). There is a PA

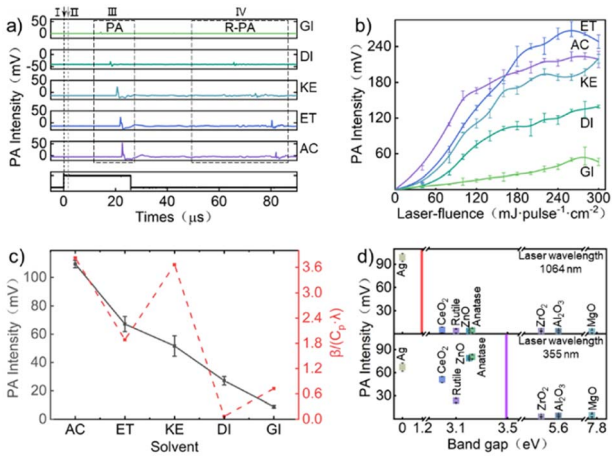

Fig. 2 (a) The PA signals of silver nanoparticles in different solvents, glycerol (GI), deionized water (DI), kerosene (KE), ethanol (ET), acetone (AC). (b) The relationship between the PA signal intensity and laser fluence of silver nanoparticles dispersed in different solvents. (c) The relationship between the thermal parameters (specific heat (C_p), thermal conductivity (λ), thermal expansion (β)) of solvents and PA intensity. (d) The intensity of the PA signal of nanoparticles with different bandgaps (dispersed in ethanol) irradiated. The red line represents the approximate photon energy of a 1064 nm wavelength laser, and the purple line represents the approximate photon energy of a 355 nm wavelength laser.

signal starting at about 14 μs (Fig. 2a(III)), and a signal of about 50 μs was the reflected photoacoustic signal (R-PA) (Fig. 2a(IV)). Under the same experimental conditions, the PA signal and R-PA signal gradually delayed with the decrease of sound velocity in the liquid medium, for example, glycerol (14 μs; 51 μs), water (18 μs; 65 μs), kerosene (20 μs; 73 μs), ethanol (21 μs; 80 μs), and acetone (22 μs; 82 μs), respectively. The relationship between the PA signal intensity and laser fluence of silver nanoparticles dispersed in different solvents is shown in Fig. 2b. It can be seen that the intensity of the PA signal increased with the increase of laser fluence. Among them, the PA signal intensity of silver nanoparticles dispersed in acetone and ethanol was the strongest, while the PA signal intensity in glycerol was the weakest. The relationship between the thermal parameters (specific heat, thermal conductivity, thermal expansion) of solvents and PA intensity is shown in Fig. 2c. It can be seen that if silver nanoparticles are dispersed in solvents with high thermal expansion coefficient, low specific heat capacity, and low thermal conductivity, relatively strong PA signals can be generated.

The intensity of the PA signal of nanoparticles with different bandgaps (dispersed in ethanol) irradiated by 355 nm and 1064 nm wavelength laser is shown in Fig. 2d. As shown in the figure, under laser irradiation at 355 nm wavelength, nanoparticles with a bandgap less than 3.5 eV (anatase, ZnO, rutile, CeO_2, Ag) generated stronger PA signals, while materials with a bandgap width exceeding 3.5 eV (ZrO_2, Al_2O_3, MgO) generated weaker PA signals. However, when choosing a 1064 nm wavelength laser to irradiate the colloidal solution of the aforementioned nanoparticles, only solutions containing silver nanoparticles can obtain strong PA signals. Although light absorption is not only related to the bandgap, the bandgap of the material is the decisive factor affecting the light absorption range of the material. Therefore, nanoparticles with a bandgap width smaller than the energy of laser photons exhibit stronger light absorption and easier absorption of laser energy. More light energy is converted into thermal energy, resulting in stronger PA signals.

Interestingly, under laser irradiation at 355 nm wavelength, although both the components of rutile and anatase were titanium dioxide and the bandgap was not significantly different (rutile ~3.0 eV, anatase ~3.2 eV), the PA intensity generated by anatase was much higher than that of rutile (Fig. 2d). The absorbed light energy of rutile was higher than that of anatase. Obviously, from the perspective of light absorption,[58] the PA signal of rutile will be stronger than that of anatase, which was contrary to the results of PA experiments. Therefore, in order to clarify the relationship between the factors that affect the intensity of PA signals, we collected the products of anatase and rutile irradiated by different laser fluences while collecting PA signals, and analyzed the crystal form and morphology of the products using SEM, TEM and Raman spectroscopy.

The changes in the crystal structure and morphology of anatase and rutile under different fluence laser irradiation are shown in Fig. 3a, b, d and e (details are provided in the ESI, Fig. S3 and S4†). When the laser fluence increased to 120 mJ per pulse per cm^2, faint peaks of rutile phase could be observed in the Raman spectrum of the irradiated anatase product (Fig. 3a(I) and (II), the characteristic Raman peaks of anatase phase are 147, 395, 520, and 639 cm^{-1}, and the characteristic Raman peaks of rutile phase are 243, 440, and 610 cm^{-1}). Raman (Fig. 3a(I) and (II)) and high-resolution transmission electron microscopy (HRTEM) (Fig. 3b(I) and (II)) analysis indicated that some anatase phases were transformed into rutile phases. When the laser fluence further increased to 160 mJ per pulse per cm^2, the Raman peak of the product was mainly in the rutile phase, and almost no obvious anatase Raman peak was observed, indicated that anatase titanium dioxide had almost transformed into rutile titanium dioxide (Fig. 3a(III) and b(III)). At 300 mJ per pulse per cm^2, anatase had been completely transformed into rutile (Fig. 3a(IV) and b(IV)). Different from anatase, although the laser fluence increased to 300 mJ per pulse per cm^2, rutile did not undergo phase transition under laser irradiation (Fig. 3e). When the laser fluence reached 60 mJ per pulse per cm^2, some spherical nanoparticles could be observed in the product, indicated that some particles began to melt (Fig. 3d(I) and (II)). When the laser fluence increased to 160 mJ per pulse per cm^2, spherical particles smaller than the size of the raw material could be observed in the product, indicated that some particles began to vaporize (Fig. 3d(III)). When the laser fluence exceeded 160 mJ per pulse per cm^2, the weakening of the Raman peak of the product indicated a decrease in crystallinity or size (Fig. 3e(III)). When the laser fluence reached 240 mJ per pulse per cm^2, the further intensification of the non-normal distribution of product size distribution may be due to evaporation (Fig. 3d(IV) and S3†).[12] These results indicate that compared to anatase, the laser threshold required for the melting and evaporation of rutile is lower.

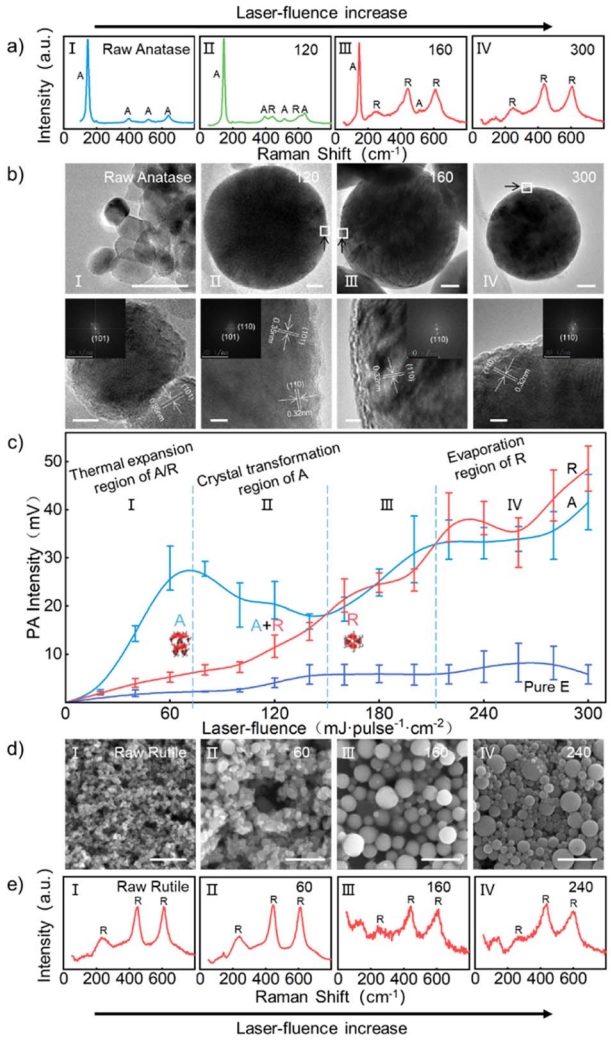

Fig. 3 Raman spectrum (a) and TEM images (b) of products of anatase under different laser fluences. (c) The relationship between the PA signal intensity and laser fluence of anatase and rutile nanoparticles in dispersed ethanol. SEM images (d) and Raman spectrum (e) of products of rutile under different laser fluences. In which A for anatase and R for rutile, and the TEM image scale is 50 nm, the HRTEM image scale is 5 nm and the SEM image scale is 500 nm.

The relationship between the PA signal intensity and laser fluence of anatase and rutile nanoparticles of the same size (~30 nm) in dispersed ethanol is shown in Fig. 3c. It can be seen that when the laser fluence was less than about 150 mJ per pulse per cm^2, the PA signal intensity of anatase titanium dioxide was stronger than that of rutile (Fig. 3c(I) and (II)). The difference in PA signal intensity between the two reached its maximum around 80 mJ per pulse per cm^2, which was mainly due to the A–R phase transition as analyzed above. When the laser fluence exceeded about 160 mJ per pulse per cm^2 until about 210 mJ per pulse per cm^2, due to the completion of the A–R phase transition of the anatase (Fig. 3a(III) and b(III)), the PA signal intensity of the two was nearly equivalent (Fig. 3c(III)). When the laser fluence was around 220 mJ per pulse per cm^2 until around 260 mJ per pulse per cm^2, rutile PA intensity than anatase indicated an increase in the weight of the effect of nanoparticles evaporation on the PA signal intensity (Fig. 3c(IV)). When the laser fluence reached 300 mJ per pulse per cm^2, anatase completely transformed into rutile, and the PA signal intensity of both increased further.

Discussion

When laser irradiates titanium dioxide/ethanol colloidal solution, titanium dioxide acts as a photothermal absorber, transferring the absorbed light energy to the surrounding liquid phase medium, causing the expansion and vaporization of the liquid phase medium (Fig. 4a). In addition to generating PA signals, liquid phase media also plays a role in transmitting PA signals. Currently, many studies have focused on the PA signals generated in liquid media.[36,51,52] In this article, based on the comparison of sound velocity, thermal conductivity, boiling point, and other aspects of liquid media, it is found that ethanol has a stronger PA signal compared to other liquid media. Moreover, the light absorption characteristics of the target material have a crucial impact on the PA spectrum. Different from commonly used photothermal absorbers such as metals (Au, Ag) and carbon, semiconductor nanomaterials with different bandgaps are used as photothermal absorbers in this article. Due to differences in bandgap, semiconductor materials have selective absorption for lasers of different wavelengths, and by changing the wavelength, the intensity of PA signal can be adjusted.

It should be considered that once the laser energy is absorbed by the nanoparticles, this energy will not only be transferred to the surrounding liquid medium, but also cause an increase in the temperature of the nanoparticles themselves. The increase in temperature of nanoparticles not only causes expansion, but also leads to crystal transformation of nanomaterials. For example, the metastable anatase chosen in this article will transform into a stable rutile phase as the temperature increases. In addition, as the laser fluence further increases, the nanoparticles will absorb enough energy and melt. Further increasing laser fluence, nanoparticles may reach

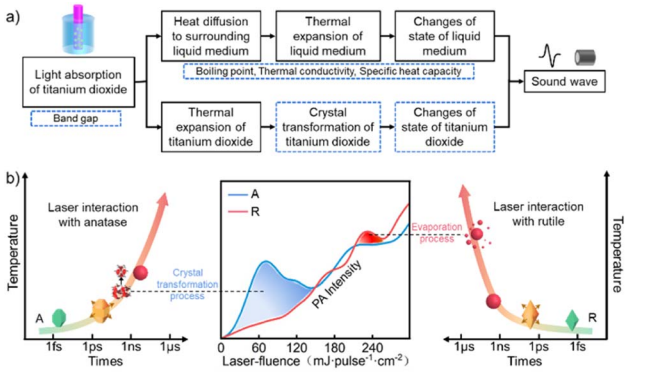

Fig. 4 (a) Energy conversion pathways during PA excitation of a colloidal suspension of nanoparticles. No color part is referenced from ref. 54. (b) Schematic diagram of the relationship between PA signal intensity and anatase phase transition and rutile evaporation.

their boiling point after absorbing sufficient energy, causing particle vaporization. However, the PA signals generated by these processes are coupled with the PA signals of liquid media, making it difficult to directly distinguish these processes from the time scale.

Thanks to the close correlation between laser fluence and the temperature that specific sized nanomaterials can reach, its quantitative relationship can be obtained through the laser melting and evaporation mechanism. Therefore, we can selectively achieve processes such as melting and vaporization of nanomaterials by controlling the laser fluence. Due to the uniqueness of laser heating, the temperatures required to expansion, phase transition, melting, and vaporization of the above-mentioned nanoparticles can be reached in the nanosecond scale. Therefore, in this article, we choose rutile with the same composition but no phase transition as a reference to analyze the effect of A–R phase transition on PA intensity. Although the thermal expansion coefficient of rutile is greater than that of anatase,[59] when the laser fluence is lower than the laser fluence required for complete A–R transformation, the PA signal of anatase is significantly stronger than that of rutile (blue area in Fig. 4b). Further increasing the laser fluence to 160 mJ per pulse per cm^2, the PA signal intensity of the anatase and rutile is almost the same after almost complete conversion of A–R. Therefore, we believe that when the laser fluence is below 160 mJ per pulse per cm^2, the stronger PA signal of anatase compared to rutile is mainly caused by the A–R phase transition. Therefore, when the laser fluence is below 160 mJ per pulse per cm^2, the stronger PA signal of anatase is mainly caused by the A–R phase transformation.

Interestingly, due to the stronger light absorption of rutile compared to anatase, the laser fluence required for the melting or vaporization of rutile is lower than that of anatase. Therefore, with further increase in laser fluence, simultaneously with the observed size change, there is a corresponding region in the spectrum of the PA signal where the rutile PA intensity is stronger than that of anatase. Therefore, as the laser fluence further increases to 220 mJ per pulse per cm^2, while observing the size change caused by vaporization, the spectrum of the PA signal also shows a region where the PA spectrum of rutile is stronger than that of rutile (red area in Fig. 4b).

It is worth discussing that it was difficult to directly distinguish the transient photothermal processes such as expansion, phase transition, melting, and evaporation of the nanoparticles in the time domain. Based on the fast laser heating process[55] (within 100 ns) and the controllable characteristics of laser fluence, on the one hand, independent acquisition of PA signals during transient photothermal processes such as expansion, phase transition, melting, and evaporation of the nanoparticles had been achieved. On the other hand, the controllable preparation of micro/nano materials and the analysis of the crystal structure and morphology of the products were achieved using the aforementioned controllable conditions. It is found that the intensity of PA signals corresponds well to the photothermal transient conditions of, phase transition, and evaporation. This enables us to detect transient processes that vary with temperature, such as phase transitions and changes in material states, in the form of laser fluence *vs.* PA signal intensity.

Conclusions

Overall, in this article, the processes of laser irradiation of micro/nano nanoparticles were investigated using PA signals excited both in surrounding liquid medium and the nanoparticles itself when tunable LSPC technology provide different photothermal conditions (such as thermal expansion, solid phase transition, and evaporation). In addition, SEM, TEM, Raman spectroscopy and other techniques were used to analyze the morphology and crystal structure of nano nanoparticles before and after laser irradiation. Finally, the relationship between the intensity of PA signals and the crystal transformation, melt spheroidization, and evaporation of nanoparticles were systematically studied. The results indicate that: (1) the intensity of the PA signal is directly proportional to the thermal expansion coefficient of the liquid medium, and inversely proportional to the specific heat and thermal conductivity. (2) Semiconductor materials with different bandgaps, as light absorbers, have the ability to selectively absorb laser beams of different wavelengths. By changing the wavelength, the PA intensity can be controlled accordingly. In addition, based on the fast laser heating and tunable fluence characteristics of non-focused laser beams in LSPC technology, transient processes such as material phase transitions and changes in physical states can be excited separately by adjusting the optical fluence. Taking titanium dioxide as an example, the PA signals generated by laser selective excitation of A–R phase transitions and rutile vaporization can be detected.

Conflicts of interest

There are no conflicts to declare.

Acknowledgements

This work was financially supported by the National Natural Science Foundation of China (no. 61805201, 52273238).

Notes and references

1 A. G. Golubovskaya, D. A. Goncharova, E. D. Fakhrutdinova, T. S. Kharlamova, O. V. Vodyankina and V. A. Svetlichnyi, *Mater. Chem. Phys.*, 2024, **314**, 128800.
2 Y. Ishikawa, T. Tsuji, S. Sakaki and N. Koshizaki, *Prog. Mater. Sci.*, 2023, **131**, 101004.
3 V. Amendola, D. Amans, Y. Ishikawa, N. Koshizaki, S. Scirè, G. Compagnini, S. Reichenberger and S. Barcikowski, *Chem.–Eur. J.*, 2020, **26**, 9206–9242.
4 D. Zhang, B. Gökce and S. Barcikowski, *Chem. Rev.*, 2017, **117**, 3990–4103.
5 P. Raveendran Nair, C. Rosa Santiago Ramirez, M. Angel Gracia Pinilla, B. Krishnan, D. Avellaneda Avellaneda, R. Fabian Cienfuegos Pelaes and S. Shaji, *Appl. Surf. Sci.*, 2023, **623**, 157096.

6 D. Ivanov, P. Shakhov, G. Tikhonowski, A. Popov, A. N. Mayorov, I. Zavestovskaya, S. Klimentov and A. V. Kabashin, *Appl. Surf. Sci.*, 2023, **643**, 158662.
7 G. Bo, H. Yu, L. Ren, N. Cheng, H. Feng, X. Xu, S. X. Dou, H. Wang and Y. Du, *ACS Appl. Nano Mater.*, 2021, **4**, 550–557.
8 X. Xu, Y. Xu, F. Xu, G. Jiang, J. Jian, H. Yu, E. Zhang, D. Shchukin, S. Kaskel and H. Wang, *J. Mater. Chem. A*, 2020, **8**, 1636–1645.
9 T. Flemban, R. Hamdi, H. Alkhabbaz, M. Alheshibri, S. Akhtar, N. Ouerfelli and K. Elsayed, *Lasers Manuf. Mater. Process.*, 2022, **9**, 18–36.
10 H. Yoshihara, N. Koshizaki, Y. Yamauchi and Y. Ishikawa, *Powder Technol.*, 2022, **404**, 117445.
11 D. Zhang, M. Lau, S. Lu, S. Barcikowski and B. Gökce, *Sci. Rep.*, 2017, **7**, 40355.
12 Y. Ishikawa, N. Koshizaki, A. Pyatenko, N. Saitoh, N. Yoshizawa and Y. Shimizu, *J. Phys. Chem. C*, 2016, **120**, 2439–2446.
13 Y. Ishikawa and N. Koshizaki, *Sci. Rep.*, 2018, **8**, 14208.
14 D. Kranz, P. Bessel, M. Rosebrock, M. Niemeyer and D. Dorfs, *Part. Part. Syst. Charact.*, 2023, **40**, 2300021.
15 H. Yu, W. Zhao, L. Ren, H. Wang, P. Guo, X. Yang, Q. Ye, D. Shchukin, Y. Du, S. Dou and H. Wang, *Adv. Mater.*, 2020, **32**, 2001571.
16 H. Yu, X. Li, L. Guo, Z. Hao, R. Zhou and X. Zeng, *RSC Adv.*, 2016, **6**, 110911–110915.
17 H. Yu, X. Li, Y. Zhu, Z. Hao and X. Zeng, *J. Phys. Chem. C*, 2017, **121**, 12469–12475.
18 Z. Swiatkowska-Warkock, A. Pyatenko, K. Koga, K. Kawaguchi, H. Wang and N. Koshizaki, *J. Phys. Chem. C*, 2017, **121**, 8177–8187.
19 Y. Ishikawa, N. Koshizaki and S. Sakaki, *J. Phys. Chem. C*, 2019, **123**, 24934–24942.
20 M. A. Mohammed, O. N. Salman and M. M. Bülbül, *Opt. Quantum Electron.*, 2023, **56**, 40.
21 H. Yu, X. Li, X. Zeng and Y. Lu, *Chem. Commun.*, 2015, **52**, 819–822.
22 M. M. Mozael, Z. Dong, A. M. Pennington, F. E. Celik, B. H. Kear and S. D. Tse, *Powder Technol.*, 2024, **431**, 119058.
23 L. B. Fachin, L. S. de Bortoli, E. Santos and D. Hotza, *Open Ceram.*, 2023, **16**, 100505.
24 A. Pyatenko, H. Wang, N. Koshizaki and T. Tsuji, *Laser Photonics Rev.*, 2013, **7**, 596–604.
25 A. Pyatenko, M. Yamaguchi and M. Suzuki, *J. Phys. Chem. C*, 2009, **113**, 9078–9085.
26 G. Soundarapandiyan, C. L. A. Leung, C. Johnston, B. Chen, R. H. U. Khan, P. McNutt, A. Bhatt, R. C. Atwood, P. D. Lee and M. E. Fitzpatrick, *Int. J. Mach. Tools Manuf.*, 2023, **190**, 104049.
27 A. Plech, V. Kotaidis, M. Lorenc and J. Boneberg, *Nat. Phys.*, 2006, **2**, 44–47.
28 O. Y. Gowayed, T. Moosa, A. M. Moratos, T. Hua, S. Arnold and B. A. Garetz, *J. Phys. Chem. B*, 2021, **125**, 7828–7839.
29 C. S. Lough, L. I. Escano, M. Qu, C. C. Smith, R. G. Landers, D. A. Bristow, L. Chen and E. C. Kinzel, *J. Manuf. Process.*, 2020, **53**, 336–341.
30 F. Babbe and C. M. Sutter-Fella, *Adv. Energy Mater.*, 2020, **10**, 1903587.
31 S. Han, Z. Sun, C. de Jacobi du Vallon, T. Collins, M. Boot-Handford, M. G. Sceats, Z. F. Tian and G. J. Nathan, *Powder Technol.*, 2022, **404**, 117459.
32 Y. Li, Y. Ye, H. Liu, R. Shen, X. Yuan, X. Miao, C. Yao, Q. Bai, L. Lu and P. Zhang, *Opt. Laser Technol.*, 2023, **157**, 108679.
33 J. E. Alba Rosales, G. Ramos-Ortiz, G. Martínez-Ponce, R. Castro-Beltrán, L. Polo-Parada and G. Gutiérrez-Juárez, *Results Phys.*, 2018, **11**, 350–357.
34 E. Huynh, B. Y. C. Leung, B. L. Helfield, M. Shakiba, J.-A. Gandier, C. S. Jin, E. R. Master, B. C. Wilson, D. E. Goertz and G. Zheng, *Nat. Nanotechnol.*, 2015, **10**, 325–332.
35 F. Garzella, P. Bianchini, A. Diaspro, A. Losi, W. Gärtner, S. Abbruzzetti and C. Viappiani, *Photoacoustics*, 2022, **26**, 100358.
36 Y. Wang, Q. Zhang, Z. Zhu, F. Lin, J. Deng, G. Ku, S. Dong, S. Song, M. K. Alam, D. Liu, Z. Wang and J. Bao, *Sci. Adv.*, 2017, **3**, e1700555.
37 J. Rodriguez-Loya, M. Lerma and J. L. Gardea-Torresdey, *Micromachines*, 2024, **15**, 24.
38 V. Amendola and M. Meneghetti, *Phys. Chem. Chem. Phys.*, 2013, **15**, 3027–3046.
39 T. Sakka, S. Iwanaga, Y. H. Ogata, A. Matsunawa and T. Takemoto, *J. Chem. Phys.*, 2000, **112**, 8645–8653.
40 H. Yu, Z. Zhang, S. Zhao, H. Wang, H. Liang, Z. Dong and X. Lin, *Opt. Laser Technol.*, 2024, **170**, 110313.
41 E. Dimitroulaki, G. J. Tserevelakis, K. Melessanaki, G. Zacharakis and P. Pouli, *J. Cult. Herit.*, 2023, **63**, 230–239.
42 A. Rosencwaig, *Anal. Chem.*, 1975, **47**, 592A–604A.
43 K. Herrmann, N. W. Pech-May and M. Retsch, *Photoacoustics*, 2021, **22**, 100246.
44 M. Kuriakose and M. A. Borden, *Curr. Opin. Colloid Interface Sci.*, 2021, **55**, 101464.
45 Y. Ma, Z. Hu, Y. Tang, S. Ma, Y. Chu, X. Li, W. Luo, L. Guo, X. Zeng and Y. Lu, *Addit. Manuf.*, 2020, **31**, 100956.
46 Y. S. Chen, W. Frey, S. Aglyamov and S. Emelianov, *Small*, 2012, **8**, 47–52.
47 K. Wilson, K. Homan and S. Emelianov, *Nat. Commun.*, 2012, **3**, 618.
48 L. Csóka, W. Hosakun, O. Kolonics and B. Ohtani, *Sci. Rep.*, 2022, **12**, 14475.
49 Y. Wang, G. Niu, S. Zhai, W. Zhang and D. Xing, *Nano Res.*, 2020, **13**, 719–728.
50 G. A. Pang, F. Poisson, J. Laufer, C. Haisch and E. Bossy, *J. Phys. Chem. C*, 2020, **124**, 1088–1098.
51 S. Wang, L. Fu, J. Xin, S. Wang, C. Yao and Z. Zhang, *J. Biomed. Opt.*, 2018, **23**, 125002.
52 M. I. P. Mendes, C. D. F. Coelho, F. A. Schaberle, M. J. Moreno, M. J. F. Calvete and L. G. Arnaut, *RSC Adv.*, 2023, **13**, 35040–35049.
53 C. Momma, B. N. Chichkov, S. Nolte, F. V. Alvensleben, A. Tünnermann, H. Welling and B. Wellegehausen, *Opt. Commun.*, 1996, **129**, 134–142.
54 G. A. Pang, J. Laufer, R. Niessner and C. Haisch, *J. Phys. Chem. C*, 2016, **120**, 27646–27656.

55 S. Sakaki and N. Koshizaki, *ChemPhysChem*, 2017, **18**, 1101–1107.
56 T. Tsuji, S. Sakaki, H. Fujiwara, H. Kikuchi, M. Tsuji, Y. Ishikawa and N. Koshizaki, *J. Phys. Chem. C*, 2018, **122**, 21659–21666.
57 M. W. Sigrist and F. K. Kneubühl, *J. Acoust. Soc. Am.*, 1978, **64**, 1652–1663.
58 J. Zhang, P. Zhou, J. Liu and J. Yu, *Phys. Chem. Chem. Phys.*, 2014, **16**, 20382–20386.
59 K. V. K. Rao, S. V. N. Naidu and L. Iyengar, *J. Am. Ceram. Soc.*, 1970, **53**, 124–126.